Exp Fluids
DOI 10.1007/s00348-010-0856-6

RESEARCH ARTICLE

Image processing for the study of bedload transport of two-size spherical particles in a supercritical flow

Virginie Hergault · Philippe Frey · François Métivier · Cécile Barat · Christophe Ducottet · Tobias Böhm · Christophe Ancey

Received: 2 December 2008 / Revised: 3 February 2010 / Accepted: 24 February 2010

Abstract Bedload sediment transport of two-size coarse spherical particle mixtures in a turbulent supercritical flow was analyzed with image and particle tracking velocimetry algorithms in a two-dimensional flume. The image processing procedure is entirely presented. Experimental results, including the size, the position, the trajectory, the state of movement (rest, rolling, and saltation), and the neighborhood configuration of each bead, were compared with a previous one-size experiment. Analysis of the solid discharge along the vertical displayed only one peak of rolling in the two-size bed, whereas three peaks of rolling appeared in the one-size case due to a larger collective motion. The same contrast is evidenced in spatio-temporal diagrams where the two-size mixtures are characterized by the predominance of saltation and a smaller number of transitions between rest and rolling. The segregation of fine particles in a bed formed by larger particles was analyzed taking into account the neighborhood configurations.

V. Hergault · P. Frey (✉) · T. Böhm
Cemagref, Unité de recherche Erosion torrentielle Neige et Avalanches, Domaine Universitaire-BP 76, 38402 St-Martin-d'Hères, France
e-mail: philippe.frey@cemagref.fr

F. Métivier
Laboratoire de dynamique des fluides géologiques IPGP/ParisVII UMR CNRS 7579, Institut de Physique du Globe de Paris, Paris, France

C. Barat · C. Ducottet
Université de Lyon, CNRS, UMR5516, Laboratoire Hubert Curien, Université de Saint-Etienne, Jean Monnet, 42000 Saint-Etienne, France

C. Ancey
Ecole Polytechnique Fédérale de Lausanne, 1015 Ecublens, Lausanne, Switzerland

1 Introduction

Sediment transport in rivers is of major importance to flood alleviation, water resource management, and environmental sustainability. In mountains, steep slopes drive intense bedload transport of a wide range of grain sizes. Bedload is the coarser transported material, remaining in contact with the bed by rolling, sliding or by saltating. Bedload transport destabilizes river channels, increases flooding problems, causing loss of property and public infrastructure, and can have adverse effects on water quality and aquatic habitat. Yet, despite a century of modern research (DuBoys 1879; Gilbert 1914), our understanding of bedload transport remains low, impairing our ability to make reliable predictions of sediment flux, even with a good knowledge of free surface water flows.

Sediment flow rates measured in natural streams are usually lower by one or two order of magnitude from the experimental flume-based bedload transport equations (Wilcock 2001; Bathurst 2007). For a better understanding of the physical mechanisms governing bedload transport, some researchers have considered bedload transport not as a continuous phase but at the scale of the particles composing the solid phase (Bridge and Dominic 1984; Wiberg and Smith 1985; Schmeeckle and Nelson 2003). As discussed recently (Frey and Church 2009), progress could be accomplished by better considering grain–grain interactions. One of the well-known reasons of the discrepancy between theory and measurements in bedload research is the problem of grain size sorting or segregation (Parker and Klingeman 1982). This phenomenon results in patterns that can be seen ubiquitously in nature such as armoring or downstream fining (see Powell 1998 for a review).

Our contribution to these issues is an experimental study of the motion of coarse spherical glass beads entrained by a

Published online: 20 March 2010

turbulent and supercritical water flow down a steep channel with a mobile bed. Using a two-dimensional channel slightly larger than the beads, we recorded from the side all bead displacements with a high-speed camera. Initially, the trajectory of a single saltating or rolling bead was analyzed (Ancey et al. 2002, 2003). The channel was then supplied continuously with beads, and measurements were taken at transport equilibrium over the mobile bed (Böhm et al. 2004; Böhm 2005). All particle trajectories were calculated by image processing (Böhm et al. 2006) allowing analysis of the fluctuations of sediment rates as well as the state of movement (rolling or saltation). These exhaustive measurements permitted a thorough statistical description of uniform sediment transport based on stochastic Markov-type processes (Ancey et al. 2006, 2008).

To advance in the understanding of grain size sorting processes, we set up new experiments using two-size mixtures. Spherical glass beads with a diameter of 4 mm together with the previously used 6-mm beads were input in the same two-dimensional channel. Building on a previous procedure for the 6-mm beads only (Böhm et al. 2006), specific image processing algorithms were developed in order to detect and track each bead, its trajectory, its state of movement, and its neighborhood configuration.

In the study of sediment transport, the use of image analysis has been steadily expanding in recent years, although not so rapidly as in general fluid mechanics, where particle image velocimetry (PIV) is now a well-established technique (see Adrian 2005 for a review). Progress has been made in suspended sediment turbulence-related issues and more recently in bedload research. Image analysis has been used in laboratories, more rarely in the field (Drake et al. 1988), to measure for instance concentrations or number of particles (Radice et al. 2006), grain size distributions and mass flux (Frey et al. 1993, 2003; Graham et al. 2005; Zimmermann et al. 2008), and particle velocities or trajectories. Tracking a single detected particle is relatively easy, and a number of authors have used image analysis to measure the trajectory of a particle in saltation (Hu and Hui 1996; Niño et al. 1994, Lee et al. 2000; Ancey et al. 2002) or in the rolling regime (Ancey et al. 2003). Tracking sediment flux is obviously more difficult. It first necessitates the segmentation of all particles and requires specific algorithms. Some steps of these algorithms are related to particle tracking velocimetry techniques (PTV).

Particle tracking velocimetry algorithms were in particular developed to track fluid tracers in flow regions where standard PIV algorithms based on cross-correlations were not well adapted because of large velocity gradients. They were also applied to track suspended sediments. Sechet and Le Guennec (1999) investigated the role of near wall turbulent structures. Their algorithm made use of a pursuit window not resolving ambiguous associations. Nezu and Azuma (2004) used PTV to characterize particle-laden-free surface flows. Their algorithm was based on the pattern matching of particle clusters between two consecutive images using invisible elastic springs, a technique described in Okamoto et al. (1995). Tracking of coarse material is rarer. Capart et al. (1997) investigated the water–sediment interaction in a dam-break release. They used a more sophisticated segmentation method and tracked the motion of 6 mm plastic beads using a predictor–corrector algorithm. Capart et al. (2002) used a pattern-based matching method using the Voronoï diagram for studying granular flows, and Spinewine et al. (2003) extended this method to stereoscopic measurements. Observing from above, Pilotti et al. (1997) analyzed dark grain incipient motion on a light smooth bed. Papanicolaou et al. (1999) using the khoros system tracked green glass beads over a layer of fixed transparent ones. In both cases, the number of particles was low, and the contrast with the bed sufficiently high to allow segmentation with simple thresholding procedures. Note that in these cases, only the motion of segmented particles could be tracked but not the entire bed. Tracking natural material without contrast and marking is very difficult. Drake et al. (1988) performed field tests with natural sediments, extracting information from the images by hand. Radice et al. (2006) evaluated sediment fluxes from above. The concentration was measured by segmenting subtracted images, a technique already used by Keshavarzy and Ball (1999). Tracking individual particles was not possible, but regional particle velocities could be assessed by PIV.

In previous studies with uniform 6-mm beads, we used a two-dimensional channel only slightly wider (6.5 mm) to be able to track all beads. For studying two-size mixtures, after numerous unsuccessful attempts, we added transparent 4-mm beads whose motion remained approximately two-dimensional and stayed in the focal plane of the camera. No background beads could be entirely concealed by foreground beads, so that all 4-mm beads could be detected and tracked.

The objective of this paper is to report the image analysis procedure developed for tracking our two-size mixtures and to present the results of the first experimental investigations analyzed with this procedure. We first present the experimental facilities and the image grabbing system in Sect. 2. In Sect. 3, we detail the image processing algorithms before presenting results in Sect. 4.

2 Experimental facilities and procedures

Experiments were carried out in a tilted, narrow, glass-sided channel, 2 m in length, already used in previous

studies (Bigillon 2001; Ancey et al. 2002; Böhm et al. 2004). Figure 1 shows a sketch of the experimental facility. The channel width W was adjusted to 6.5 mm. The particle diameters were 4 and 6 mm. Even with the 4-mm beads, the particle motion remained approximately two-dimensional. The channel slope tan θ was set to 12.5% for the three experiments presented in this paper. To prevent crystallographic arrangements, the steel channel base consisted of half-cylinders of equal size (radius of 3 mm), randomly arranged on different levels, from 0 to 5.5 mm, by increments of 0.5 mm. These levels were generated using a sequence of uniformly distributed random numbers.

Black spherical glass beads with a nominal diameter of 6 mm (provided by Sigmund Lindner GmbH, Germany) and transparent spherical glass beads of diameter 4 mm (provided by Cimap, France) both with a density ρ_p of 2,500 kg/m^3 were used. The black beads were input from a reservoir into the channel using a wheel driven by a direct current motor and equipped with 20 hollows on the circumference. The transparent beads were input with a vibrating device allowing the beads to fall on a ramp leading to the channel inlet. The water supply at the channel entrance was controlled by an electromagnetic flow meter (provided by Krohne, France).

Two experiments with a two-size mixture are presented together with a 6-mm one-size case for comparison. Parameters relative to the three experiments are summarized in Table 1. For the one-size 6-mm bead experiment N12-16 (Böhm 2006; Fig. 2), the input rate $\dot{n}_6$ was 15.1 beads per second, with an uncertainty of less than 5%. The case M12-8-18 is a mixture of 64% by weight of 6-mm beads and 36% of 4-mm beads. The input rates were $\dot{n}_6 = 8.1$ beads/s for the 6-mm beads and $\dot{n}_4 = 18.0$ beads/s for the 4-mm beads. For the 4-mm beads, an uncertainty of 15% on the solid rate was measured. In the experiment M12-14-1, 4-mm beads represented only 1% of the mixture. The input rates were $\dot{n}_6 = 13.5$ beads/s and $\dot{n}_4 = 0.5$ beads/s. The total volumic solid discharge per unit width was calculated according to $q_s = \pi/6W\,(6^3\,\dot{n}_6 + 4^3\,\dot{n}_4) \times 10^{-9}$. These three experiments at the same slope of 12.5% were selected for comparison, because they had approximately the same total volumic solid discharge ($q_s = 0.23$–0.26×10^{-3} m^2/s).

Table 1 Flow and bedload characteristics and time-averaged values of dimensionless numbers. N12-16 is the one-size case, M12-8-18 and M12-14-1 the two-size mixture cases

Experiment	N12-16	M12-8-18	M12-14-1
tan θ (%)	12.5	12.5	12.5
$\dot{n}_6$ (beads/s)	15.1	8.1	13.5
$\dot{n}_4$ (beads/s)		18.0	0.5
q_s (10^{-3} m^2/s)	0.26	0.23	0.24
q_w (10^{-3} m^2/s)	3.85	7.66	3.65
C_s (%)	7.0	3.0	6.5
h (mm)	8.2	15.2	8.6
u_f (m/s)	0.47	0.50	0.42
Re	4360	5398	4004
Fr	1.66	1.30	1.45
h/d	1.4	3.0	1.4
$2h/W$	2.5	4.7	2.6

The hydraulic conditions can be specified using classic dimensionless numbers (Table 1). The flow Reynolds number is defined as $\mathrm{Re} = 4R_h u_f/\nu$, where $R_h = Wh/(2h + W)$ denotes hydraulic radius, h the averaged flow depth, $u_f = q_w/h$ the averaged fluid velocity, q_w the water

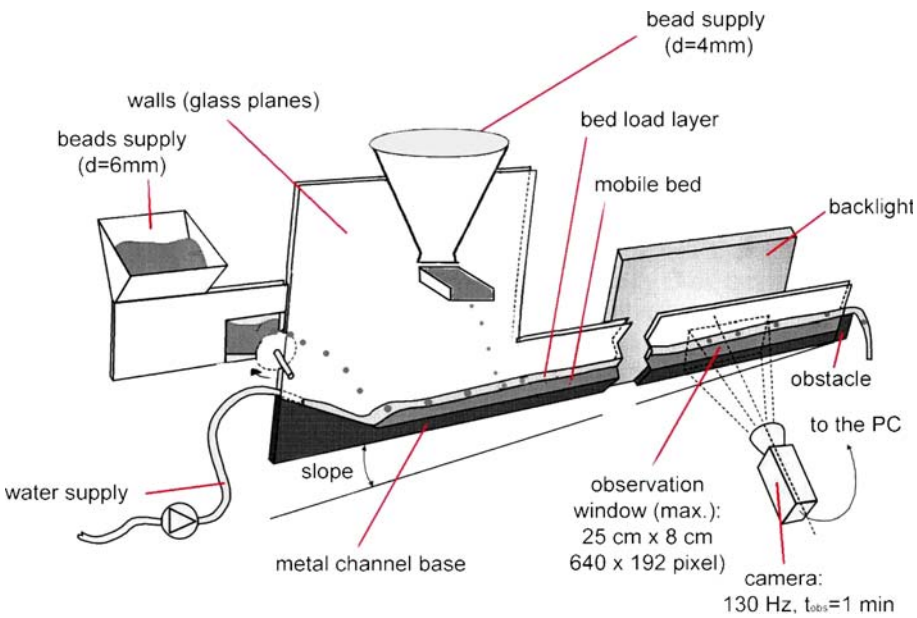

Fig. 1 Sketch of the experimental arrangement (modified from Böhm et al. 2004)

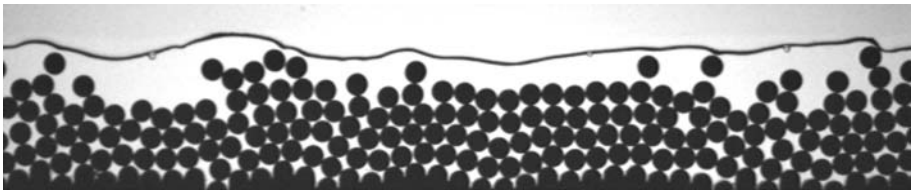

Fig. 2 Image corresponding to the one-size case N12-16 with 6-mm beads

discharge per unit width, and ν the kinematic viscosity of water. The Froude number $\mathrm{Fr} = u_f/\sqrt{gh}$ (where g denotes gravity acceleration) was always greater than 1 (supercritical flow). The solid transport concentration is defined as the ratio of the solid and the water discharge $C_s = q_s/q_w$. The instantaneous water depth was defined as the difference between the water and the bed elevation. The water free surface elevation was obtained by image analysis (see Sect. 3.3). The bed elevation profile is the broken line linking the top points of the uppermost resting or rolling beads (see Sects. 3.2, 3.3). Rolling particles were included because they had a very low velocity compared to the mean water velocity. The instantaneous water depth was averaged spatially (within one image) and temporally over the sequence to obtain the average water depth. A conservative uncertainty estimate of the water depth is 1 pixel (0.387 mm) which implies for the uniform run (N12-16) a relative value of 5%. The mean velocity was calculated from the flow discharge which was very constant (0.5%). However, independent measurements were taken with a dye method (Recking et al. 2008a) similar to the salt dilution method and proved consistent with calculated values (Dufresne 2005).

The mean dimensionless number values differ substantially from the values usually found in the hydraulics literature. The reason is twofold: first we used a narrow channel, which led to studying low Reynolds number regimes, whereas in most experiments on bed load transport, one takes care to avoid such regimes; this is the price to pay to have access to the details of particle movements. However, despite the unusual features of our experimental device, the mean velocity profile and the main features of the turbulence were not too far from those typically observed in larger flumes (Frey and Reboud 2001; Ancey et al. 2002, 2003). Therefore, we think that the small size of the experimental setup is not a handicap. Second, we studied supercritical flows because of the steep slopes investigated. However, in a supercritical regime, flow depth was low (on the order of the particle size), meaning that particle motion could be affected by the water free surface.

All experiments were filmed using a Pulnix partial scan motion camera (progressive scan TM-6705AN). The camera was placed perpendicular to the glass panes at a distance of 115 cm from the channel, approximately 80 cm upstream from the channel outlet. It was inclined at the same angle as the channel. Lights were positioned in the backside of the channel. A new high bright white LED back-light device (provided by Phlox, France) was used to ensure a uniform and stable lighting especially for the detection of the 4-mm transparent beads. An area of approximately 25 cm in length and 8 cm in height was filmed and later reduced to accelerate image processing. The camera resolution was 640 × 192 pixels for a frame rate of 131.2 frames per second (exposure time: 0.2 ms, 256 gray levels). Each sequence was limited to 8,000 images due to limited computer memory. This corresponded to an observation duration of approximately 1 min. Each experiment was repeated at least twice in order to trace possible experimental problems and to gain an idea of data scattering.

The procedure used to reach equilibrium with the two-size mixture M12-8-18 was very similar to the one reported in (Böhm et al. 2006) for uniform bead experiments. First of all, a particle bed was built along the channel base, which remained stationary on average. To that end, an equilibrium between the water discharge, solid discharge, bed elevation, and channel slope was sought. By transport equilibrium, we mean that there was no more bed degradation nor aggradation over a sufficiently long time interval. This equilibrium was reached by using the following procedure:

- The water discharge was set to a constant value.
- An obstacle was set at the channel outlet to enable bed formation and prevent full bed erosion. The solid discharges at the channel entrance were set to constant values. The channel was initially empty with only the steel bottom. The bed was built progressively by injecting the beads from the two reservoirs. The first beads supplied by the feeding system were stopped by the obstacle at the channel outlet and started to form a bed. The bed line rose to the level of the obstacle, and beads began to leave the channel. After approximately 10 min, the system arrived at bed load equilibrium.
- In order to make the bed line parallel with the channel base, the water discharge was then adjusted. After several iterations, we arrived at the configuration with the bed line slope matching the channel base inclination. Average equilibrium conditions were sustained over long time periods, as long as 30 min.

Input of the two-size mixture M12-8-18 resulted in a bed mainly formed by the 4-mm beads (Fig. 3), contrasting with the one-size case (Fig. 2), although the 6-mm bead

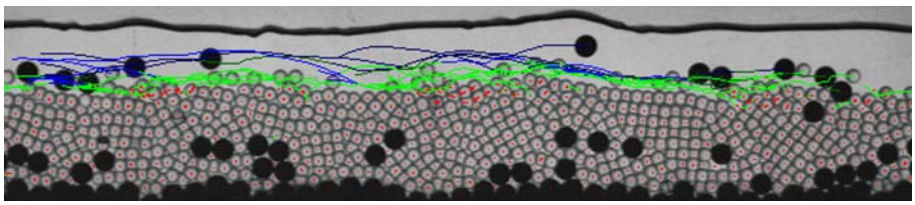

Fig. 3 Thirtieth image of the two-size mixture M12-8-18 with superimposed trajectories corresponding to the first 30 images (*dark* and *light blue trajectories* represent saltation for, respectively, 6- and 4-mm beads, *dark* and *light green trajectories* represent rolling for, respectively, 6- and 4-mm *beads*, and *red trajectories* represent *beads* at rest)

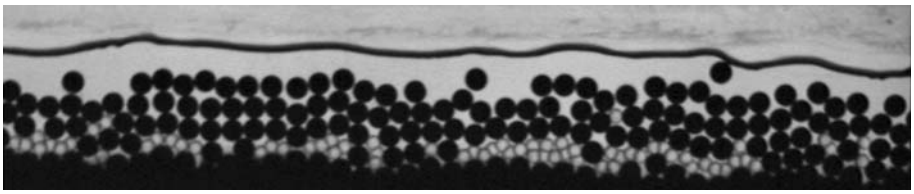

Fig. 4 Image corresponding to the two-size mixture M12-14-1

solid discharge represented 64% by weight of the total. In order to better understand the movement of 4-mm beads in the bed initially composed of 6-mm beads, we set up a specific experiment (M12-14-1). Once bed equilibrium was reached with the 6-mm beads (experiment N12-16), we input the 4-mm beads one by one (the input rate was actually 0.5 bead per second), approximately 70 cm upstream of the field of view. We observed qualitatively by eye the progressive sinking of some 4-mm beads. A 1-min image sequence was acquired after 20 min (Fig. 4).

3 Image processing

The experimental system described above recorded high-speed numerical image sequences. The aim of image processing was to determine, from the 8,000 image sequence, all trajectories and states of movement of each bead. For the present study, we used the image processing platform Wima (Ducottet 1994) developed by the Hubert Curien laboratory (University of Saint Etienne, France). Written in C++ under Windows and Linux, Wima is composed of a graphical user interface and an image processing library. It provides fundamental operations of preprocessing, segmentation, measurement on 2D, 3D images, or image sequences, as well as more specific operations such as PIV or tracking tools.

Processing the new temporal image sequences containing the two different types of beads raised several problems compared to the unimodal case. We extended the previously proposed algorithm (Böhm et al. 2006) to include the detection of the transparent beads and the analysis of the neighborhood of the beads. We first recall the initial algorithm, and second we detail the extended version adapted to two-size mixtures.

3.1 Initial algorithm

The initial algorithm (Böhm et al. 2006) was adapted to process the uniform spherical black beads. It was composed of three main steps:

1. Particle detection and localization, consisting in detecting all the beads in each image and determining the position of their centers;
2. Reconstruction of particle trajectories, consisting in tracking the beads along the sequence to obtain a set of trajectories;
3. Determination of the state of movement, consisting in analyzing, for each position in trajectories, if the bead is rolling, saltating, or resting.

The first step can be considered as a pattern-matching problem in a gray scale image (Gonzalez and Woods 2008; Barat et al. 2003). The detection used a correlation method with a ring-shape model of the bead (Fig. 5b). The correlation coefficient image contained peaks at each matching point between the model and a bead (Fig. 5c). Local maxima of the different peaks gave the location of the searched beads (Fig. 5d).

In the second step, the problem of tracking particles along a temporal sequence was addressed. It is known as the point tracking problem in the literature. Usually, points can be either small object centroids or interest points in larger rigid or unrigid objects. Depending on the application and on the assumptions made on point displacement, more or less complex approaches have been proposed (Sethi and Jain 1987; Hwang 1989; Salari and Sethi 1990). A particular application known as PTV is to determine the velocity field of a fluid carrying small particles (Nishino et al. 1989; Economikos et al. 1990; Fayolle et al. 1996; Udrea et al. 2000). In our study, we focused on the

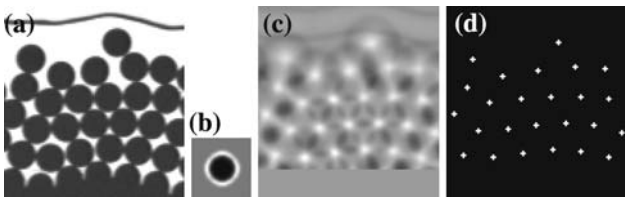

Fig. 5 **a** Initial image with *black beads*, **b** the image model, **c** correlation result, **d** positions of *black bead* centers

individual particle motions. Particle velocities differed from those of the surrounding fluid, since our particles were coarse and had a higher density than water.

Taking as input particle position data, our algorithm constructs the whole set of trajectories. It uses the principle of prediction to select candidates for an association and the minimal distance criteria to choose the best one. The best associations were obtained by a greedy approach similar to the method proposed by Rangarajan and Shah (1991). An estimate for the particle position in the second image was obtained by adding the displacement vector of the preceding calculation step to each particle position in the first image. Although the use of spherical particles of the same size made detection easier, the calculation of the trajectories was more difficult, since we were unable to distinguish particles based on their shape. Moreover, the trajectories consistency criteria classically used in PTV were not valid due to beads collisions. Thanks to the high frame rate of the camera, the displacement of a particle between two images was generally (but not always) smaller than a particle diameter. This was essential not only to reach a high resolution of the trajectories, but primarily to achieve a good accuracy with the tracking algorithm.

In the third step, the state of movement was determined according to the following criteria:

- Resting beads were those whose velocity u_p (averaged over five consecutive frames) was lower than a threshold velocity u_t.
- Rolling beads remained in close contact with the bed. Their velocity verified $u_p > u_t$ and their distance d_n to the nearest neighbor verified the condition $d_n/d < \varepsilon$. ε was fixed to 1.07, and the reference distance d was the diameter of the beads.
- Saltating beads made small hops above others and had no close neighbors except near collisions; the beads not at rest and not rolling were considered in saltation.

3.2 Extended algorithm

In the new experimental setup, images contained two different types of beads, the previous 6-mm opaque black beads mixed with transparent 4-mm ones. The previous algorithm had to be extended to take into account the second type of beads. The two first steps could be addressed independently for each type of bead. On the contrary, the third step had to be modified because the state of movement of a bead depends on whether neighbors are of the same diameter or not. In addition, a fourth step was developed to determine the state of movement of neighboring bead configurations located along the four diagonals. The proposed new algorithm can be broken down as follows:

1. Detection and localization of the two types of beads independently;
2. Reconstruction of trajectories of black and transparent beads independently;
3. Determination of the state of movement with the bead mixture;
4. Analysis of the neighborhood of the beads.

The first step was the most difficult one. The black beads could be detected with the same procedure as the initial algorithm, but the transparent ones required a particular processing since they did not appear as a uniform disk. A transparent bead appeared indeed as a faint dark ring whose shape depended on the transversal position of the bead in the channel and on its other neighboring beads. We used a morphological operator *hconvex* (or *h-domes)* (Vincent 1993; Soille 1999) to detect the local regional maxima produced at the center of beads. To limit false detections, we combined the *hconvex* operator with additional pre and postprocessing. The entire processing of transparent beads is presented in Sect. 3.3.

The second step was simply achieved using the initial reconstruction algorithm applied independently on black and transparent beads positions. We finally obtained two tables with the trajectories of, respectively, all black and transparent beads. Depending on the solid discharge adjusted at the channel entrance, the black table contained about 400–2,000 trajectories and the transparent table about 8,000–10,000. Figure 3 gives an example of an image with superimposed trajectories.

In the third step, the state of movement was determined using the initial criteria adapted to the case of the two types of beads. Therefore, the distance d_n of rolling beads to the nearest neighbor verified the modified condition $d_n/d^* < \varepsilon$ where the reference distance d^* was fixed to the minimum distance according to the diameters of the bead and its nearest neighbor. It can take three different values depending on the relative diameters of the couple of these beads: black–black ($d^* = 6$ mm), black–transparent ($d^* = 5$ mm) and transparent–transparent ($d^* = 4$ mm).

Finally, in the fourth step, the neighborhood configuration was determined by analyzing the type of the four neighbors of a bead located in each of the four quadrants defined in Fig. 6a. A candidate bead for a specific quadrant

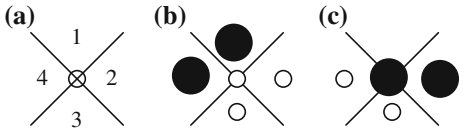

Fig. 6 Neighborhood configurations

was considered to be a neighbor of the bead under analysis if it was the nearest neighbor in this quadrant and if its distance d_n from the bead verified $d_n/d^* < \eta$. The constant η is fixed to 1.14 to provide a tolerance on the distance. If no bead verified these conditions, no neighbors were selected, and the quadrant remained void. Figure 6 presents a possible neighborhood configuration for transparent (b) and black (c) beads.

3.3 Detection of transparent beads

The detection principle of transparent beads relied on the morphological operator *hconvex* (or *h-domes)* (Vincent 1993; Soille 1999). This operator can detect local maxima whose height is higher or equal to h. For a given gray scale image f, and a given height h, it is defined as:

$$\mathrm{Hconvex}_h(f) = f - R_f^{\delta}(f-h)$$

The operator $R_f^{\delta}(f-h)$ represents the reconstruction by dilation of the image f from the marker image $f-h$. It is obtained as the geodesic dilation of $f-h$ with respect to f iterated until stability. Figure 7 illustrates the operator Hconvex applied on a one-dimensional digital signal. The result (Fig. 7c) shows non null values that form peaks at the location of maxima. The peaks of height h represent maxima of the same height. Then, a threshold of this image at level h (Fig. 7d) gives the location of maxima of height at least h.

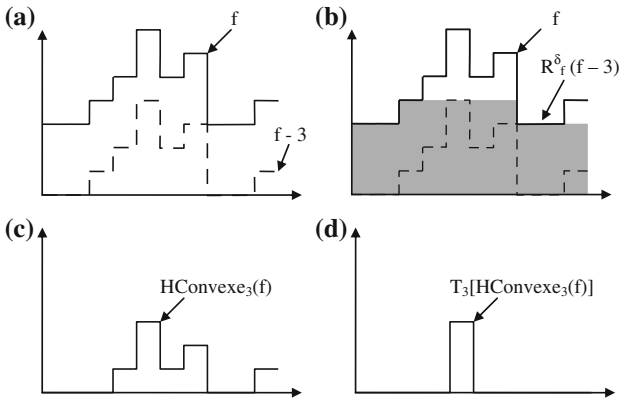

Fig. 7 Hconvex operator illustrated on a 1D profile for $h = 3$. **a** The 1D profile f and its translated $f-3$, **b** the reconstruction by dilation $R_f^{\delta}(f-3)$, **c** Hconvex $_3(f) = f - R_f^{\delta}(f-3)$, **d** thresholding of Hconvex $_3(f)$ at threshold 3

The entire detection procedure of transparent beads consisted of four steps illustrated in Fig. 8:

1. removing the previously detected black beads by replacing them using a morphological closure of the image (Fig. 8b);
2. applying the *hconvex* operator (Fig. 8c);
3. detecting transparent beads after thresholding the *hconvex* image (Fig. 8d);
4. postprocessing to remove maxima located in the background of the image (Fig. 8e).

In the first step, we began with building a mask to detect the black beads with an appropriate thresholding of the initial image. We also computed the morphological closure of the initial image to reconstruct the background at the location of black beads. The two obtained images are combined to replace, in the original image (Fig. 8a), the black beads with the reconstructed background (Fig. 8b). In the second step, the *hconvex* operator was applied after a smoothing of the resulting image of step 1 with a gaussian filter of standard deviation of 1 pixel. Given a reference height h, the *hconvex* operator detected all the local maxima of height greater than or equal to h. The value of h had to be adjusted to select relevant local maxima. In the third step, we selected relevant regional maxima by thresholding the *hconvex* image at the value h. The fourth step is a postprocessing step combining selection operations to remove false detections located above the water free surface and outside the region containing transparent beads.

To detect the water line, a top hat operator was first applied to the original image (Fig. 9a), the resulting image was thresholded, and finally a thinning was applied (Fig. 9b). The top hat was calculated by taking the difference between the image and the morphological closure of this image (Serra 1982). To detect the region containing transparent beads, we applied a Sobel gradient operator to the image without the black beads (Fig. 9c), we thresholded the result, and we applied a closing to fill holes and an opening to remove small regions (Fig. 9d).

4 Results

Results presented in this section serve two purposes: the first, perhaps the most important in this paper is to illustrate the capabilities of our image processing procedure. The second is to provide insights into bedload transport at the particle scale. The first Sect. (4.1) is devoted to global variables, namely water depth and transport concentration. In the following Sects. 4.2 and 4.3, the contrasted one-size N12-16 and two-size M12-8-18 experiments are compared making full use of image analysis results. The next section

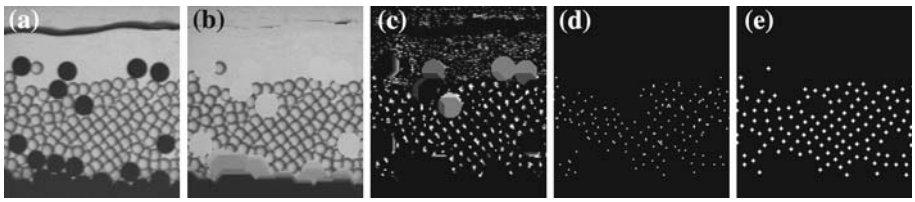

Fig. 8 Main steps of the transparent bead detection algorithm **a** initial image, **b** replacement of *black beads* with background, **c** *hconvex* operator result, **d** thresholding of image (**c**), **e** final result after deleting spurious maxima

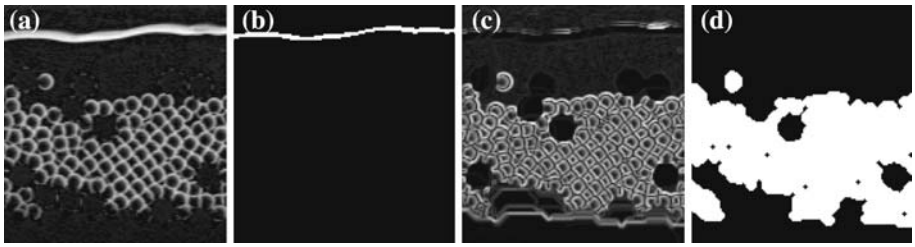

Fig. 9 Detection of both the *water line* and the *transparent beads* region. In Fig. 8e, all the maxima located *above* the *water line* and *outside* the *transparent beads* region were removed. **a** Result of the *top* hat applied to the original image (Fig. 8a), **b** the *water line* obtained after thresholding and thinning, **c** result of the Sobel gradient applied to the image without the *black beads* (Fig. 8b) **d** the *transparent beads* region obtained after closing and opening

analyses segregation occurring in run M12-14-1 (very low input flux of small beads). The last section provides a neighborhood analysis for both two-size runs.

4.1 Water depth and transport concentration

Contrary to the 6-mm bead unimodal case in which motion was perfectly two-dimensional (Fig. 2), 4-mm beads in the 6.5-mm channel exhibited a tendency to blockage because of the ratio 4 mm compared to 6.5 mm. When equilibrium was reached (experiment M12-8-18), the bed was mainly formed by less mobile 4-mm beads (Fig. 3). As a result, flow resistance was greater with 4-mm beads generating a higher water depth. For approximately the same solid discharge ($q_s = 0.23$–0.26×10^{-3} m^2/s), it was necessary to input a water discharge twice as great as in the unimodal case N12-16, meaning that the concentration C_s was divided by a factor 2 (Table 1). Of course, a higher water depth also meant more dissipation on the transparent walls of the flume. However, the use of an Einstein type side wall correction (Frey et al. 2006) still resulted in bed resistance coefficients higher with this two-size mixture than with 6-mm beads. In our case, the structure of the two-size mixture had a stronger effect than the lower *h*/*d* ratio (Recking et al. 2008b).

For the case M12-14-1, the solid and water discharges were approximately the same as the case N12-16. The concentration C_s was slightly lower, and the water depth slightly higher than the experiment N12-16. In this experiment (M12-14-1), the mixture was still principally composed by 6-mm beads in the uppermost layers with only a few 4-mm beads at the bottom (Fig. 4). Therefore, the 4-mm beads had a very weak influence on the water flow and the bed load.

4.2 Solid discharge vertical profiles

The distributions of q_s along the vertical together with the contributions of saltation and rolling to the total solid discharge are plotted for the one-size N12-16 experiment (Fig. 10a) and the M12-8-18 two-size experiment (Fig. 10b), respectively. It is to be noted that the contribution of resting beads was not equal to zero because of vibration resulting in low movement not considered as rolling. Therefore, the total solid discharge may be higher than the added contributions of rolling and saltation.

Figure 10a shows three peaks at intervals of approximately one particle diameter corresponding to three peaks of rolling. There is only one peak for saltation approximately equal to the uppermost rolling peak at the same location ($y = 32$ mm), adding together to form the uppermost total peak. This profile thus clearly indicates that the particle bed had a layered structure and the two uppermost bed layers ($y = 20$ and 26 mm) were prone to rolling.

On Fig. 10b, the same distributions are broken down according to the size fraction. There is also only one peak of saltation for the two types of particles. By contrast to the unimodal case, there is only one rolling peak at a slightly lower position than the saltation peak. It indicates that the motion of rolling particles was only possible on the layer near to the bed surface. Indeed, the 4-mm beads formed an imbricated bed preventing large movement of the bed layers.

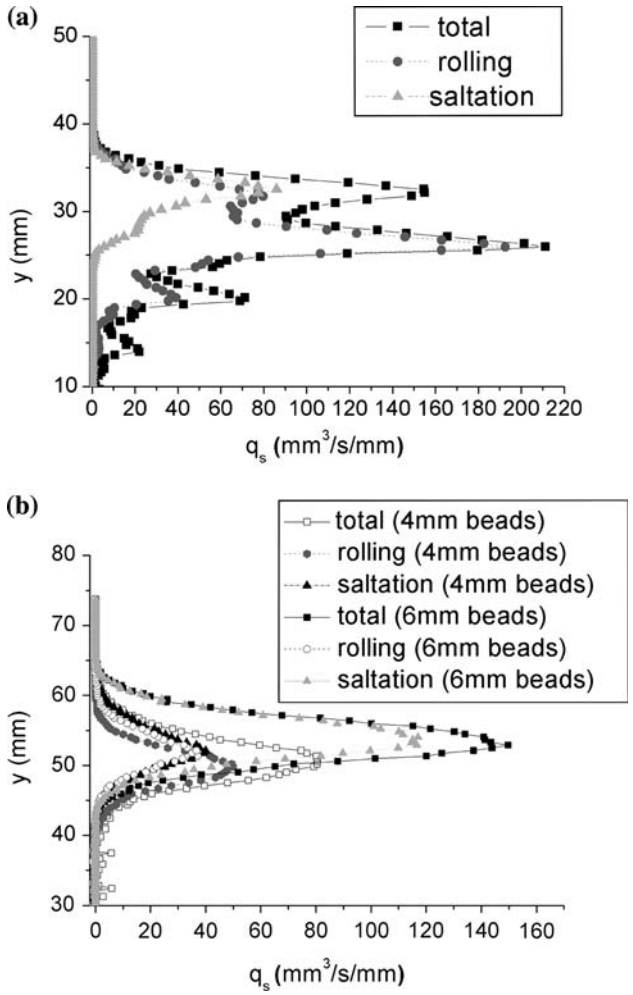

Fig. 10 Solid discharge vertical profiles (total solid discharge and elementary contributions) for **a** the one-size N12-16 case, **b** the two-size mixture M12-8-18

4.3 Bead propagation

In order to study the spatio-temporal bead propagation, we plotted the particle movement in the (x, t)-plane for the unimodal case N12-16 (Fig. 11) and for the two-size mixture M12-8-18 (Fig. 12a, b). x is the streamwise abscissa and t the time. Only beads in saltation (black lines) and rolling (gray lines) are presented, beads at rest have been omitted for the sake of clarity. Beads entered the observation window on the left and departed on the right. The time propagation is downwards. Since the x-component of the velocity of a bead is the ratio between the x-displacement and the elapsed time, it is equivalent to the inverse of the slope of the trace. Since beads moved faster in the saltating regime than in the rolling regime, the slope of the trace corresponding to saltating beads is lower than for rolling. Only 4 s out of the entire 60-s sequence are represented. The events presented here were nevertheless typical of the entire experiments.

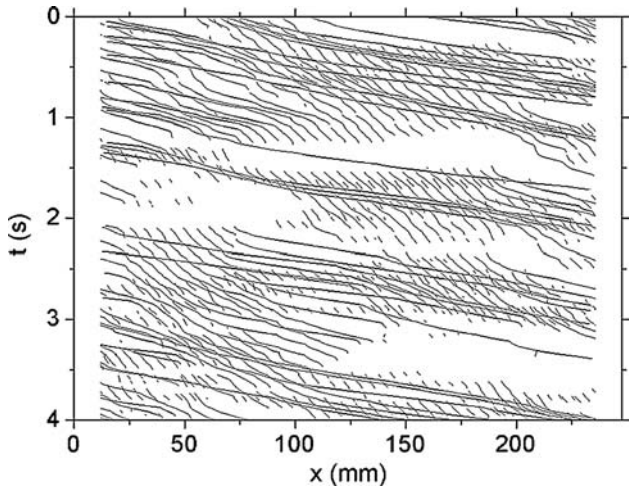

Fig. 11 Bead propagation in the plane (x, t) for the one-size N12-16 case. *Black lines* represent beads in saltation and *gray lines* rolling beads

The unimodal case (Fig. 11) is mainly characterized by the collective motion of rolling beads as evidenced by a series of gray streaks. This phenomenon was modeled by Ancey et al. (2008).

In the two-size case, the beads were more frequently in the saltating regime than in the unimodal case. Especially, the larger beads of the two-size mixture were essentially in saltation with only a little part of their trajectory in the rolling regime. The beads typically travelled distances as long as the window length. Indeed, Fig. 12a shows that transitions from rolling to saltation (or from saltation to rolling) were rare and there were no beads switching between rest and rolling. The same phenomenon was predominant for the 4-mm beads even if the transitions from rolling to saltation were more frequent, and there were a few beads switching between rest and rolling (see Fig. 12b at $x \sim 50$ mm, $t \sim 0.6$ s). However, the phenomenon of collective rolling motion was not obvious with the two-size mixture and appeared specific to the unimodal case.

The low proportion of transitions in the two-size mixture is certainly due to fewer exchanges between the bead layers. As already described in Sect. 4.2, only the uppermost bed layer had the capacity to move because of the imbricated bed formed by the 4-mm beads. By contrast, in the unimodal case, the rather loose bed packing formed by 6-mm beads allowed the motion of rolling particles in several bed layers.

4.4 Segregation of smaller beads

Since input of a solid flux composed of about one-third of small beads resulted in a bed mainly formed by the same small beads, the purpose of the run M12-14-1 was to analyze the movement of 4-mm beads. To that end, a very low solid flux of 4-mm beads was input into the flow

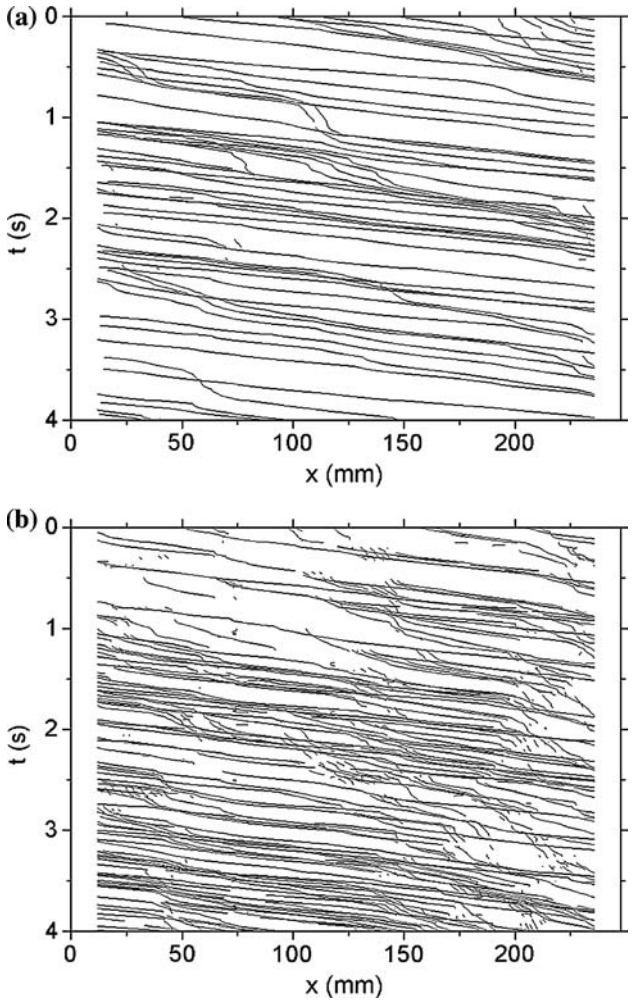

Fig. 12 Bead propagation in the plane (x, t) for the two-size mixture M12-8-18, **a** 6-mm beads, **b** 4-mm beads. *Black lines* represent beads in saltation and *gray lines* rolling beads

initially formed only of larger moving beads (N12-16). This very low flux (1% of the total flux) first enabled us to quietly visualize the segregation process and second permitted to virtually keep the same water flux. Progressively, a number of 4-mm beads sank through the moving larger beads until reaching the steel bottom and forming a quasi-continuous layer of transparent beads, 20 min after small bead input (Fig. 4). This segregation process may be similar to the "kinetic sieving" process described in dry granular flows (Savage and Lun 1988; Thomas 2000; Hill and Zhang 2008). It is, however, only a hypothesis at this stage. This segregation process is very rapid in dry granular experiments performed with rotating drum or heap experiments. By contrast, although in our experiments it only took a few seconds for a saltating particle to travel from input to the downstream end of our field of view, 20 min were required to reach the state of Fig. 4 which means that the timescale of segregation, presumably a kinetic sieving process, is larger by 2–3 orders of magnitude than saltation.

4.5 Transition between rolling and rest

In this part, we investigate the transitions between rolling and rest. These transitions are the most important phenomena in bed load transport because they correspond to erosion and deposition on the bed. In Tables 2 and 3, we represent the three most favorable neighborhood configurations responsible for the transitions "rolling to rest" (C10) and "rest to rolling" (C01) for both the M12-8-18 and the M12-14-1 experiments. We give also the rate of beads in each neighborhood configuration compared to the total number of configuration for the considered transition (C01 or C10). Note that the configurations are represented by a cross. In each quadrant, the presence or the absence of a bead defines the neighborhood of the studied bead. The large black disks symbolize the 6-mm beads and the small white disks the 4-mm beads. It must also be specified that in the observation window, the water flowed from left to right.

Table 2 (M12-8-18 case) indicates that, for 4-mm beads, the configuration with large beads downstream was favorable to rest. Regarding the liftoff, except the first configuration maybe due to false detections, 6-mm beads in the neighborhood were also favorable to rolling of 4-mm beads. In fact, the large beads were essentially on the upper

Table 2 Representation of the three most favorable configurations of neighborhood responsible for the transition rest to rolling (C01) and the transition rolling to rest (C10) with their percentage rate (M12-8-18 experiment)

		C10			C01		
4mm beads	percents	8%	7%	7%	10%	9%	8%
	conf.	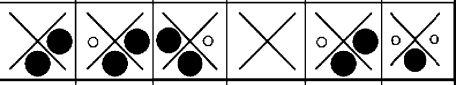					
6mm beads	percents	22%	11%	10%	12%	11%	10%
	conf.	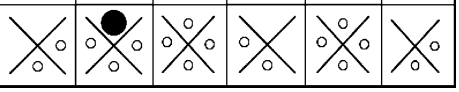					

Table 3 Representation of the three most favorable configurations of neighborhood responsible for the transition rest to rolling (C01) and the transition rolling to rest (C10) with their percentage rate (M12-14-1 experiment)

		C10			C01		
4mm beads	percents	10%	10%	9%	14%	14%	13%
	conf.	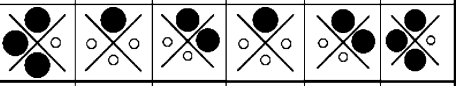					
6mm beads	percents	24%	23%	14%	25%	24%	15%
	conf.	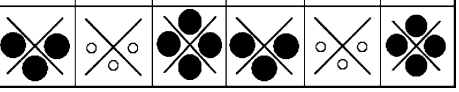					

layer above a bed mainly formed by a 4-mm bed. Four-millimeter rolling beads were only possible on the layer near the free surface and were thus frequently in interaction with the 6-mm beads.

For the 6-mm beads (M12-8-18 case), the configuration with a bead downstream and below led principally to rest and the configuration with a bead upstream and below led principally to rolling, which is coherent with the direction of the flow. More specifically, the transition rest to rolling was mainly caused by 4-mm beads. Indeed, when a 6-mm bead came to rest, which was very rare, fine particles accumulated behind them promoting its liftoff.

In the M12-14-1 experiment (with a very small rate of 4-mm beads), the 4-mm beads migrated downward and began to form a layer at the bottom. Nevertheless, the bed was still predominantly formed by 6-mm beads (see Fig. 4). Table 3 indicates that for the 4-mm beads, the three main neighborhood configurations leading to the transitions C01 and C10 were the same, that is, four beads in the neighborhood. Indeed, most of 4-mm beads that arrived in the observation window stopped, restarted again, but finally migrated in the bed down to the bottom. Only a few of them travelled distances as long as the window length. They were switching from rolling to rest and from rest to rolling in the uppermost bed layers. That is why, presumably, the favorable neighborhood configurations for these transitions were the cases with four beads in the neighborhood.

For the 6-mm beads of the M12-14-1 case, the most favorable neighborhood configurations for the transitions C10 and C01 were also the same, that is, three or four large beads in the neighborhood. All 6-mm beads were prone to rolling. They formed a layered structure allowing the movement of beads in all bed layers contrary to the imbricated bed of 4-mm beads preventing movement of bed layers. Furthermore, collective motion was very important for 6-mm beads, which could explain these neighborhood configurations.

5 Conclusions and perspectives

Building on a previous method adapted to one-size particles, we have detailed a new image processing procedure combining different algorithms and solutions into a single original method handling experiments with two-size mixtures. Given a temporal sequence of images, it is possible to determine the size, the position, the trajectory, the state of movement, and the neighborhood configuration of each bead. Building a processing chain to process two-size mixtures is not trivial, and two major challenges have been addressed: the detection of the two types of beads and the analysis of their state of movement depending on the neighboring configurations.

This procedure was successfully applied to bed load transport of two-size mixtures (4- and 6-mm diameter beads). We first compared a two-size mixture (case M12-8-18 with an input flow composed of about one-third by weight of smaller particles) with previous results obtained with uniform 6-mm beads in the same flume. When equilibrium was reached, the bed was mainly formed by 4-mm beads because of downward migration of the fine particles.

The distributions of the solid discharge along the vertical, together with the contributions of saltation and rolling, showed very different patterns between the unimodal case and the two-size mixture. In the unimodal case, three peaks of rolling could be distinguished at intervals of about one particle diameter, indicating a rather loose bed packing allowing the movement of beads in the uppermost bed layers. By contrast to the unimodal case (N12-16), there was only one rolling peak in the two-size case, indicating that the 4-mm beads formed an imbricated bed preventing movement of the bed layers.

Based on spatio-temporal analysis, we showed that both 6- and 4-mm beads were essentially in saltation with few beads switching between the saltation and the rolling regimes. Only the fine particles had a few trajectories mainly in the rolling regime with transitions from rest to rolling. By contrast, in the one-size case, the collective motion of rolling particles was predominant, and the transitions from rest to rolling and vice versa were very frequent. The layered structure of 6-mm beads and the imbricated bed of 4-mm beads described previously explain these observations.

In an attempt to understand the downward migration of the smaller particles, a very low 4-mm bead flux was added to the 6-mm flux, and input to a bed initially only composed of moving 6-mm beads. We evidenced a segregation process similar to the kinetic sieving process largely described in granular flows, but implying longer timescales.

Finally, analysis of the transitions between rest and rolling taking into account the bead neighborhood was performed for both two-size experiments. For the M12-8-18 experiment, the 4-mm beads were principally stopped by 6-mm downstream beads, whereas 6-mm beads began to roll because of fine particles accumulating upstream. Regarding the 4-mm beads in the experiment M12-14-1, the transitions were principally caused by a neighborhood of four beads. Indeed, most of the 4-mm beads migrated inside the bed and moved in the loose bed of 6-mm beads.

The segregation process evidenced in our experiments opens up numerous perspectives. Of course, other experiments will be necessary to study all stages of the transition between uniform-sized and two-sized experiments, taking advantage of the image processing procedure, especially the study of small bead trajectories.

It can be objected that our specific very narrow experimental channel limits the generality of our results. We note, however, that in recent experiments made with bimodal mixtures of natural gravel material in a wide channel, the same segregation phenomenon was observed (Recking et al. 2009) whereby the small particles were sinking through the moving coarser particles. Segregation is an ubiquitous phenomenon in granular flow whether driven by gravity only or by a shearing fluid. Altogether, it appears that a good basis exists in the physics of granular flows to improve our understanding of bedload transport either experimentally or theoretically. Furthermore, we think that the analysis of the neighborhoods responsible for the transitions, only possible thanks to this very complete image processing procedure, will prove to be a powerful tool to analyze further experiments and to give results easily comparable to discrete models based on cellular automata or molecular dynamics.

Acknowledgments This study was supported by *Cemagref* and funding was provided by *Institut National des Sciences de l'Univers* and *Agence Nationale de la Recherche* through grants ANR-05-ECCO-015 and ANR GESTRANS.

References

Adrian RJ (2005) Twenty years of particle image velocimetry. Exp Fluids 39:159–169

Ancey C, Bigillon F, Frey P, Lanier J, Ducret R (2002) Saltating motion of a bead in a rapid water stream. Phys Rev E 66:036306

Ancey C, Bigillon F, Frey P, Ducret R (2003) Rolling motion of a bead in a rapid water stream. Phys Rev E 67:011303

Ancey C, Böhm T, Jodeau M, Frey P (2006) Statistical description of sediment transport experiments. Phys Rev E 74:011302 (Part 1)

Ancey C, Davison AC, Böhm T, Jodeau M, Frey P (2008) Entrainment and motion of coarse particles in a shallow water stream down a steep slope. J Fluid Mech 595:83–114

Barat C, Ducottet C, Jourlin M (2003) Pattern matching using morphological probing. In: IEEE international conference on image processing. Barcelona, pp 369–372

Bathurst JC (2007) Effect of coarse surface layer on bed-load transport. J Hydraul Eng-ASCE 133:1192–1205

Bigillon F (2001) Etude du mouvement bidimensionnel d'une particule dans un courant d'eau sur forte pente, PhD Dissertation Université Joseph Fourier, Grenoble, p 217

Böhm T (2005) Motion and interaction of a set of particles in a supercritical flow, PhD dissertation, Université Joseph Fourier, Grenoble I, p 172

Böhm T, Ancey C, Frey P, Reboud JL, Ducottet C (2004) Fluctuations of the solid discharge of gravity-driven particle flows in a turbulent stream. Phys Rev E 69:061307

Böhm T, Frey P, Ducottet C, Ancey C, Jodeau M, Reboud J-L (2006) Two-dimensional motion of a set of particles in a free surface flow with image processing. Exp Fluids 41:1–11

Bridge JS, Dominic DF (1984) Bed load grain velocities and sediment transport rates. Water Resour Res 20:476–490

Capart H, Liu HH, VanCrombrugghe X, Young DL (1997) Digital imaging characterization of the kinematics of water-sediment interaction. Water Air Soil Pollut 99:173–177

Capart H, Young DL, Zech Y (2002) Voronoï imaging methods for the measurement of granular flows. Exp Fluids 32:121–135

Drake TG, Shreve RL, Dietrich WE, Whiting PJ, Leopold LB (1988) Bedload transport of fine gravel observed by motion-picture photography. J Fluid Mech 192:193–217

DuBoys M (1879) Le Rhône et les rivières à lit affouillable. Annales Ponts et Chaussées Serie 5 XVIII:141–195

Ducottet C (1994) Application of wavelet transforms to the processing of tomographic and holographic images of fluid flow, PhD Dissertation, University of Saint Etienne, France

Dufresne M (2005) Etude expérimentale du transport de particules solides par charriage à forte pente, unpublished Master's thesis, ULP/ENGEES (in French), 91

Economikos L, Shoemaker C, Russ K, Brodkey RS, Jones D (1990) Toward full-field measurements of instantaneous visualizations of coherent structures in turbulent shear flows. Exp Thermal Fluid Sci 3:74–86

Fayolle J, Ducottet C, Fournel T, Schon JP (1996) Motion characterization of unrigid objects by detecting and tracking feature points. In: IEEE 1996 international conference on image processing. Lausanne, pp 803–806

Frey P, Church M (2009) How river beds move. Science 325:1509–1510

Frey P, Reboud JL (2001) Experimental study of narrow free-surface turbulent flows on steep slopes. In: Ninokata H, Wada A, Tanaka N (eds) Advances in flow modeling and turbulence measurements. World Scientific Publishing Co., Singapore, pp 396–403

Frey P, Morel R, Champagne JY, Gay B (1993) Hydrodynamics fields and solid particle transport in a settling-tank. J Hydraul Res 31:763–776

Frey P, Ducottet C, Jay J (2003) Fluctuations of bed load solid discharge and grain size distribution on steep slopes with image analysis. Exp Fluids 35:589–597

Frey P, Dufresne M, Böhm T, Jodeau M, Ancey C (2006) Experimental study of bed-load on steep slopes. River flow 2006, Lisbonne, Portugal, 6–8 Sept, Balkema, pp 887–893

Gilbert GK (1914) The transportation of débris by running water. Professional paper 86, U.S. Geological Survey, Washington, DC

Gonzalez RC, Woods RE (2008) Digital image processing, 3rd edn. Prentice-Hall, Englewood Cliffs

Graham DJ, Reid I, Rice SP (2005) Automated sizing of coarse-grained sediments: Image-processing procedures. Math Geol 37:1–28

Hill KM, Zhang J (2008) Kinematics of densely flowing granular mixtures. Phys Rev E 77:061303

Hu CH, Hui YJ (1996) Bed-load transport.1. Mechanical characteristics. J Hydraul Eng-ASCE 122:245–254

Hwang VSS (1989) Tracking feature points in time-varying images using an opportunistic selection approach. Pattern Recogn 22:247–256

Keshavarzy A, Ball JE (1999) An application of image processing in the study of sediment motion. J Hydraul Res 37:559–576

Lee HY, Chen YH, You JY, Lin YT (2000) Investigations of continuous bed load saltating process. J Hydraul Eng ASCE 126:691–700

Nezu L, Azuma R (2004) Turbulence characteristics and interaction between particles and fluid in particle-laden open channel flows. J Hydraul Eng ASCE 130:988–1001

Niño Y, Garcia M, Ayala L (1994) Gravel saltation 1. Experiments. Water Resour Res 30:1907–1914

Nishino K, Kasagi N, Hirata M (1989) Three-dimensional particle tracking velocimetry based on automated digital image processing. Trans ASME J Fluid Eng 111:384–391

Okamoto K, Hassan YA, Schmidl WD (1995) New tracking algorithm for particle image velocimetry. Exp Fluids 19:342–347

Papanicolaou AN, Diplas P, Balakrishnan M, Dancey CL (1999) Computer vision technique for tracking bed load movement. J Comput Civil Eng 13:71–79

Parker G, Klingeman PC (1982) On why gravel bed streams are paved. Water Resour Res 18:1409–1423

Pilotti M, Menduni G, Castelli E (1997) Monitoring the inception of sediment transport by image processing techniques. Exp Fluids 23:202–208

Powell DM (1998) Patterns and processes of sediment sorting in gravel-bed rivers. Prog Phys Geogr 22:1–32

Radice A, Malavasi S, Ballio F (2006) Solid transport measurements through image processing. Exp Fluids 41:721–734

Rangarajan K, Shah M (1991) Establishing motion correspondence. Comput Vis Graph Image Process Image Underst 54:56–73

Recking A, Frey P, Paquier A, Belleudy P, Champagne J-Y (2008a) Bed-load transport flume experiments on steep slopes. J. Hydraul Eng-ASCE 134:1302–1310

Recking A, Frey P, Paquier A, Belleudy P, Champagne J-Y (2008b) Feedback between bed load transport and flow resistance in gravel and cobble bed rivers. Water Resour Res 44:W05412

Recking A, Frey P, Paquier A, Belleudy P (2009) An experimental investigation of mechanisms involved in bed load sheet production and migration. J Geophys Res Earth Surf 114:F03010

Salari V, Sethi IK (1990) Feature point correspondence in the presence of occlusion. IEEE Trans Pattern Anal Mach Intell 12:87–91

Savage SB, Lun CKK (1988) Particle-Size Segregation in Inclined Chute Flow of Dry Cohesionless Granular Solids. J Fluid Mech 189:311–335

Schmeeckle MW, Nelson JM (2003) Direct numerical simulation of bedload transport using a local, dynamic boundary condition. Sedimentology 50:279–301

Sechet P, Le Guennec B (1999) The role of near wall turbulent structures on sediment transport. Water Res 33:3646–3656

Serra J (1982) Image Analysis and Mathematical Morphology. Vol. 1. Academic Press, New York

Sethi IK, Jain R (1987) Finding trajectories of feature points in a monocular image sequence. IEEE Trans Pattern Anal Mach Intell (PAMI) 9:56–73

Soille P (1999) Morphological image analysis: principles and applications. Springer, Berlin

Spinewine B, Capart H, Larcher M, Zech Y (2003) Three-dimensional Voronoï imaging methods for the measurement of near-wall particulate flows. Exp Fluids 34:227–241

Thomas N (2000) Reverse and intermediate segregation of large beads in dry granular media. Phys Rev E 62:961–974

Udrea D, Bryanston-Cross P, Querzoli G, Moroni M (2000) Fluid mechanics and its application: chapter particle tracking velocimetry techniques. Kluwer, Dordrecht, pp 279–304

Vincent L (1993) Morphological grayscale reconstruction in image analysis: Applications and efficient algorithms. EEE Trans Image Process 2:176–201

Wiberg PL, Smith JD (1985) A theoretical model for saltating grains in water. J Geophys Res C 90:7341–7354

Wilcock PR (2001) Toward a practical method for estimating sediment-transport rates in gravel-bed rivers. Earth Surf Process Land 26:1395–1408

Zimmermann AE, Church M, Hassan MA (2008) Video-based gravel transport measurements with a flume mounted light table. Earth Surf Process Land 33:2285–2296